On the receptivity of surface plasma actuation in high-speed boundary layers

Article *in* Physics of Fluids · September 2020

DOI: 10.1063/5.0016508

Physics of Fluids

On the receptivity of surface plasma actuation in high-speed boundary layers

Cite as: Phys. Fluids **32**, 094102 (2020); https://doi.org/10.1063/5.0016508
Submitted: 05 June 2020 . Accepted: 13 August 2020 . Published Online: 01 September 2020

Yutian Wang (王宇天), Yiwen Li (李益文), Jianxin Liu (刘建新), and Yinghong Li (李应红)

ARTICLES YOU MAY BE INTERESTED IN

Analysis of the effect of intermittency in a high-pressure turbine blade
Physics of Fluids **32**, 095101 (2020); https://doi.org/10.1063/5.0018679

Ultrafast tomographic particle image velocimetry investigation on hypersonic boundary layers
Physics of Fluids **32**, 094103 (2020); https://doi.org/10.1063/5.0014168

Passive and active control of turbulent flows
Physics of Fluids **32**, 080401 (2020); https://doi.org/10.1063/5.0022548

Physics of Fluids ARTICLE scitation.org/journal/phf

On the receptivity of surface plasma actuation in high-speed boundary layers

Cite as: Phys. Fluids 32, 094102 (2020); doi: 10.1063/5.0016508
Submitted: 5 June 2020 • Accepted: 13 August 2020 •
Published Online: 1 September 2020

View Online Export Citation CrossMark

Yutian Wang (王宇天),[1] Yiwen Li (李益文),[1] Jianxin Liu (刘建新),[2,a)] and Yinghong Li (李应红)[1]

AFFILIATIONS

[1] Science and Technology on Plasma Dynamics Laboratory, Air Force Engineering University, 710038 Xi'an, People's Republic of China
[2] Department of Mechanism, School of Mechanical Engineering, Tianjin University, 300072 Tianjin, People's Republic of China

[a)] **Author to whom correspondence should be addressed:** shookware@tju.edu.cn

ABSTRACT

Significant amounts of work have been conducted in the area of plasma flow control, while the receptivity of plasma actuation in high-speed boundary layers has not had much attention over the last two decades. In the present study, the receptivity of a Mach 4.5 flat-plate boundary layer to plasma heating actuation produced by pulsed-DC surface dielectric barrier discharge (SDBD) has been studied by direct numerical simulation (DNS) and stability analysis. With the help of multimode decomposition technology, the amplitude of normal modes can be obtained. The results show that both fast and slow modes can be excited by plasma actuation, and the receptivity maximum is observed near the lower neutral branch. Because the pulsed-DC SDBD actuation is typical periodic pulse signals, when the total power remains constant, the Fourier components with multiples of actuation frequency have the same energy, regardless of the waveform, period, and width of the actuation signal. Such characteristics benefit the robustness of the pulsed-DC SDBD actuator. A theoretical prediction method by combining the receptivity model and linear parabolized stability equations is considered in the present study, and good agreement with the DNS results is achieved.

I. INTRODUCTION

Since the heat transfer, skin friction, and flow separation are much different in laminar and turbulent boundary layers, the laminar–turbulent transition plays a critical role in the design and optimization of super/hypersonic vehicles. On the one hand, laminar flow is expected to be maintained on the entire surface of vehicles, which benefit from the low skin friction drag and heat transfer in laminar flow. Especially for hypersonic vehicles, the weight of the Thermal Protection System (TPS) can be significantly reduced. On the other hand, for air-breathing scramjet vehicles, e.g., X-43/51 series, turbulent flow can help to eliminate flow separation on the forebody inlet induced by the shockwave and boundary layer interaction as well as enhance the mixture of fuel and air for improving combustion efficiency. Therefore, the accurate prediction and control of boundary layer transition are of great significance to improve the performance of the super/hypersonic vehicles.

Laminar–turbulent transition in the high-speed boundary has been studied for more than 50 years; excellent reviews of this research have been conducted by Fedorov,[1] Zhong and Wang,[2] and Lee and Chen.[3] Nevertheless, it is still difficult to obtain an analytical solution of the transition position at even a simple flat-plate boundary layer. The most important reason is that the transition process is strongly dependent on the external environmental conditions, such as noise, temperature fluctuation, turbulence, and surface roughness. Morkovin *et al.*[4] and Reshotko[5] summarized five main paths to the transition. Among them, path A corresponding to nature transition is most likely to occur in real flight conditions, where the level of environmental disturbances is usually low. The natural transition process can be divided into five stages, including receptivity, linear modal growth, nonlinear interactions, secondary instability, and breakdown to turbulence. When disturbances' amplitude increases to a modest level, transient growth,[6] arising from the non-normality of disturbance equations, may become important before linear modal growth (refer to path B in Ref. 4).

As the first stage in the transition process, receptivity determines the amplitude, frequency, and phase of eigenmodes, which was first proposed by Morkovin.[7] For the two-dimensional subsonic boundary layer, the research on receptivity is focused on the scale-conversion mechanism, since wavelength scales of external disturbances are essentially different from those of Tollmien–Schlichting (TS) waves. The excellent theoretical works were conducted by Goldstein,[8] Ruban,[9] Zhigulev and Fedorov,[10] and Choudhari and Streett,[11] also see the work of Goldstein and Hultgren[12] as well as the work of Saric *et al.*[13] for reviews. When the Mach number Ma_∞ is larger than about 4 for an adiabatic wall, besides the first mode associated with the TS waves, higher modes become dominant, which is usually called Mack mode.[14] They are inherently inviscid instabilities and belong to a family of trapped acoustic waves.[1]

In the early experiments by Kendall[15] and Stetson *et al.*,[16] there were large disturbances observed near the leading edge, where no growing disturbance was expected according to linear stability theory (LST). The first breakthrough research on these findings was conducted by Fedorov and Khokhlov.[17] They found that there were two modes near the leading edge whose phase velocities are close to those of fast ($1 + 1/Ma_\infty$) and slow ($1 - 1/Ma_\infty$) acoustic waves, respectively. These modes were also studied by Ma and Zhong;[18] in addition to the first and the second modes, they named the stable modes as modes I, II, etc. For consistency of the following discussions, the terminology suggested by Fedorov and Tumin[19] is employed in this paper. In the leading-edge vicinity, the two modes, named fast mode (mode F) and slow mode (mode S), can be directly excited through a strong interaction with the fast and slow acoustic waves instead of the scale-conversion mechanism. The slow mode is usually unstable in most cases and essentially the first mode, whereas the fast mode is stable. When the phase velocity of the fast mode is gradually reduced to 1, it can be synchronized with the freestream entropy or vorticity waves. Further downstream, the phase speeds of the fast and slow modes are approaching or equal to the position near the neutral branch of the second mode. A strong interaction between the synchronized modes occurs due to the nonparallel effects; as a result, one mode becomes the unstable second mode, and oppositely, the other becomes more stable. The leading edge receptivity coefficients predicted by Fedorov[20] show good agreement with the experimental results of Maslov *et al.*[21] Such receptivity theory is also validated with direct numerical simulation (DNS) by Ma and Zhong,[18,22] Mailk and Balakumar,[23] Egorov *et al.*,[24] and Balakumar.[25]

In addition to the natural receptivity, there is another important type of receptivity, named forced receptivity.[26] The forced receptivity is referred to the mechanism by which the instability mode is directly excited by the wall surface actuation source, such as periodic blow-suction, local heating or cooling, vibrations, and plasma actuation, which is the focus of this article.

Fedorov and Khokhlov[27] conducted theoretical research on the receptivity of the hypersonic boundary layer to three types of wall disturbances with asymptotic analysis. They found that the hypersonic boundary layers are more sensitive to vertical velocity perturbations than temperature perturbations, and the maximum receptivity coefficient occurs in the vicinity of the branch point near the lower neutral branch of the second mode. Such results are consistent with those of Pralits *et al.*[28] using the adjoint parabolized stability equations (APSEs). They also demonstrated that the maximum control yield can be obtained if the wall or momentum forcing is close to the lower branch of the neutral stability curve in low Ma_∞ (up to 1.2) compressible boundary layers. Wang and Zhong[29,30] gave a specific focus on the receptivity of the hypersonic boundary layer to the blow-suction actuation. They found that the instability mode is strongly excited when the actuator is located upstream of the synchronization point. The DNS computations can provide complete information on boundary layer receptivity, instability, and even transition. However, theoretical analysis is required to understand and interpret the leading physical mechanisms behind a messy disturbance field. For gaining insight into the numerical simulation data, a multimode decomposition method was proposed by Tumin[31,32] and Gaydos and Tumin,[33] which is based on the biorthogonal eigenfunction system. Tumin *et al.*[34,35] applied multimode decomposition to filter out stable and unstable modes coexisting in DNS results, and a good agreement with the receptivity predicted model[36] is reached.

Plasma flow control[37,38] is different from the traditional mechanical technology. Non-equilibrium plasma can be produced by gas discharge, in which the rapid transformation from electric energy to the internal and kinetic energy of the fluid is achievable, through the interaction between charged particles and neutral gas molecules. Recently, a series of studies on the control of the crossflow-induced transition in the subsonic boundary layer with the plasma actuator have been conducted by Dörr and Kloker[39] and Guo and Kloker.[40,41] Based on the concept named upstream flow deformation (UFD), subcritical crossflow vortex modes can be excited by the body force produced by the plasma actuators, and the transition is delayed through hindering the growth of the most amplified crossflow mode. Schuele *et al.*[42] and Arndt *et al.*[43] experimentally studied the excitability of crossflow modes by an azimuthal array of micrometer-sized plasma actuators in the three-dimensional super/hypersonic boundary layers. For high-speed flat-plate boundary layers, Keller *et al.*[44] conducted a numerical study on the potential of local energy deposition mimicking the plasma discharge as transition-triggering devices. The effect of base-flow manipulation on the growth of the second mode is investigated, while the receptivity of plasma actuation still needs to be addressed.

A comprehensive understanding of the receptivity mechanism can help us make proper decisions on transition control strategies, and so the research on the receptivity of surface plasma actuations in high-speed boundary layers is conducted in this paper. The remainder of this paper is structured as follows: The basic governing equations of DNS and stability analysis as well as the new schemes of the multimode decomposition and receptivity model are introduced in Sec. II. Section III starts with a code validation, and then, the numerical modeling of plasma actuation is given. The detailed computational results and comparison with the theoretical prediction are presented in Sec. IV. Finally, conclusions are drawn in Sec. V.

II. PROBLEM FORMULATION AND NUMERICAL METHODS

A. Direct numerical simulations

The equations governing the total flow are the full compressible Navier–Stokes (NS) equations, and the flow and coordinate quantities are made non-dimensional as follows:

$$\begin{cases} x = \dfrac{x^*}{\delta_0^*}, y = \dfrac{y^*}{\delta_0^*}, z = \dfrac{z^*}{\delta_0^*}, t = \dfrac{t^* U_\infty^*}{\delta_0^*}, u = \dfrac{u^*}{U_\infty^*}, v = \dfrac{v^*}{U_\infty^*}, w = \dfrac{w^*}{U_\infty^*}, \\ \rho = \dfrac{\rho^*}{\rho_\infty^*}, p = \dfrac{p^*}{\rho_\infty^* U_\infty^{*2}}, T = \dfrac{T^*}{T_\infty^*}, \mu = \dfrac{\mu^*}{\mu_\infty^*}, \kappa = \dfrac{\kappa^*}{\kappa_\infty^*}, \end{cases} \tag{1}$$

where the variables with superscript $*$ and subscript ∞ represent the dimensional and far-field flow quantities, respectively. In addition, the boundary layer length scale δ_0^* at a specific location, introduced to normalize the coordinates, and the reference Reynolds number Re_0 are defined as

$$\delta_0^* = \left(\frac{\mu_\infty^* x_0^*}{\rho_\infty^* U_\infty^*}\right)^{\frac{1}{2}}, \quad Re_0 = \frac{\rho_\infty^* U_\infty^* \delta_0^*}{\mu_\infty^*}. \tag{2}$$

The dynamic viscosity μ is computed by the Sutherland law, and the thermal conductivity κ is prescribed with a constant Prandtl number. Based on the Stokes hypothesis and the calorically perfect gas assumption, the dimensionless compressible NS equations could be written in the conservative form

$$\frac{\partial U}{\partial t} + \frac{\partial E}{\partial x} + \frac{\partial F}{\partial y} + \frac{\partial G}{\partial z} + \frac{\partial E_v}{\partial x} + \frac{\partial F_v}{\partial y} + \frac{\partial G_v}{\partial z} + \mathcal{F}(U_B) = S_p(x, y, z, t), \tag{3}$$

where U is the conservative flux, E, F, and G are the vectors of convective flux, and E_v, F_v and G_v indicate the viscosity terms. In the present numerical studies, we restrict our attention to the two-dimensional flows over a smooth flat plate, and the compressible similarity solutions are used as base flows whose solver has been validated.[45] Since the similarity solutions are not the stationary solution of the full NS equations, the term $\mathcal{F}(U_B)$ is introduced to maintain the basic flows, and such a method has been adopted in many studies.[46,47] $S_p(x, y, z, t)$ is the source term of plasma actuation, and the detailed description is given in Sec. III.

The DNS computation code used for the present work is developed from the parallel high-order finite difference solver named OpenCFD. This original solver was developed by Li *et al.*[48,49] and has been used widely in many papers. As the receptivity of small disturbance is concerned, there is no strong shockwave discontinuity over the whole flow field. The convection terms are split by using Stager–Warming splitting and are discretized with a ninth-order upwind scheme, whereas the viscous terms are discretized with a tenth-order center scheme. The third-order total variation diminishing-type (TVD) Runge–Kutta method is used for the time advance.

B. Stability analysis

The disturbance equations are obtained through the decomposition of the flow quantities into disturbance q' and steady basic flow q_0. For small disturbances, neglecting the nonlinear terms, the linearized disturbance equations are presented in the following compact form:

$$\begin{aligned} &\Gamma\frac{\partial q'}{\partial t} + A\frac{\partial q'}{\partial x} + B\frac{\partial q'}{\partial y} + C\frac{\partial q'}{\partial z} + Dq' \\ &= V_{xx}\frac{\partial^2 q'}{\partial x^2} + V_{yy}\frac{\partial^2 q'}{\partial y^2} + V_{zz}\frac{\partial^2 q'}{\partial z^2} + V_{xy}\frac{\partial^2 q'}{\partial x \partial y} + V_{xz}\frac{\partial^2 q'}{\partial x \partial z} \\ &\quad + V_{yz}\frac{\partial^2 q'}{\partial y \partial z}, \end{aligned} \tag{4}$$

where the coefficient matrices are functions of the base flows and can be found in Appendix A.

In the quasi-parallel linear stability theory (LST) approximation, the solution of the linearized disturbance equations is considered in the form of normal modes,

$$q'(x, y, z, t) = \hat{\phi}(y)\exp(i\alpha x + i\beta z - i\omega t) + c.c., \tag{5}$$

where $\hat{\phi} = (\hat{\rho}, \hat{u}, \hat{v}, \hat{w}, \hat{T})^T$ represents the vector of the disturbance shape function, and the superscript T stands for transpose. α and β indicate the streamwise and spanwise wavenumbers, respectively, while the angular frequency is denoted by ω. Substituting Eq. (5) into the linear disturbance equations (4), the full Eigen equation of spatial mode can be recast as follows:

$$\mathcal{L}_0 + \alpha\mathcal{L}_1\hat{\phi} + \alpha^2\mathcal{L}_2\hat{\phi} = 0. \tag{6}$$

The operators $\mathcal{L}_0$, $\mathcal{L}_1$, and $\mathcal{L}_2$ are given in Appendix B. Such a nonlinear eigenvalue problem can be circumvented by a simple linear transformation

$$\mathrm{H}_0\Phi = \alpha\mathrm{H}_1\Phi, \tag{7}$$

$$\mathrm{H}_0 = \begin{bmatrix} \mathcal{L}_0 & \mathcal{L}_1 \\ 0 & -\mathrm{I} \end{bmatrix}, \quad \mathrm{H}_1 = \begin{bmatrix} 0 & -\mathcal{L}_2 \\ -\mathrm{I} & 0 \end{bmatrix}, \quad \Phi = \begin{bmatrix} \hat{\phi} \\ \alpha\hat{\phi} \end{bmatrix} \tag{8}$$

(for more details, see Ref. 50). In the present work, the global spectrum is computed by using the Chebyshev polynomials collocated and the standard QZ algorithm, which provide a good guess of the eigenvalue for local computations. For the local spectrum, the tenth-order center difference and the Arnoldi method are employed. For the eigenvalue problem of discrete modes, the Dirichlet conditions boundary conditions at the wall and far-field are imposed,

$$\begin{cases} \hat{u} = \hat{v} = \hat{w} = \hat{T} = 0 & at\, y = 0, \\ \hat{u} = \hat{v} = \hat{w} = \hat{T} = 0 & at\, y \to \infty. \end{cases} \tag{9}$$

The parabolized stability equations (PSEs) account for the nonparallel effect due to the boundary layer growth and are used to predict the linear evolution of disturbances in the boundary layer. In the linear PSE formulation, following the suggestion by Herbert,[51] the disturbances are expressed as

$$q'(x,y,z,t) = \hat{\phi}(\xi,y)exp\left(i\int_{x_0}^{x}\alpha(\xi)d\xi + i\beta z - i\omega t\right) + c.c. \quad (10)$$

Here, $\hat{\phi}$ is a function of $\xi = \epsilon x$, $\epsilon = O(\mathrm{Re}^{-1})$, i.e., it is a slow function of x. Substituting the ansatz [Eq. (10)] into the linear disturbance equations (4) and retaining terms up to order $O(\mathrm{Re}^{-1})$, one can obtain the linear PSE equations as

$$\hat{A}\frac{\partial\hat{\phi}}{\partial x} + \hat{B}\frac{\partial\hat{\phi}}{\partial y} + V_{yy}\frac{\partial^2\hat{\phi}}{\partial y^2} + \hat{D}\hat{\phi} = 0. \quad (11)$$

The operators $\hat{A}$, $\hat{B}$, and $\hat{D}$ were given by Zhang and Zhou.[52] The residual ellipticity of the PSE is due to the term $\partial\hat{p}/\partial x$ of the streamwise momentum equations that have been discussed by Li and Malik[53] and Andersson *et al.*,[54] and the method proposed by Chang and Malik[55] is used in the present PSE calculations. The normal direction discretization method and the boundary condition are the same as those of the local LST, whereas a simple second-order backward finite difference scheme is employed to discretize the streamwise direction.

C. Multimode decomposition

In this paper, a simple biorthogonal multimode decomposition scheme is developed to analyze messy perturbations among boundary layers. This method is essentially consistent with those proposed by Tumin[31,32] and Gao and Luo.[56] Since the LST system is not self-adjoint, its eigenfunctions of the eigenvalue problem and the corresponding adjoint equation comprise a biorthogonal eigenfunction system. Therefore, the decomposition coefficients can be evaluated with the help of an orthogonality relation. The inner product between two arbitrary functions is defined according to

$$\langle A,B\rangle = \int_0^\infty A^T B dy. \quad (12)$$

Provided α_n is the eigenvalue corresponding to the eigenfunction Φ_n and α_m is the eigenvalue corresponding to the eigenfunction Ψ_m of the adjoint equation, with the help of the inner product definition, the process of deducing the orthogonal relationship is given as follows:

$$\begin{cases} \langle\Psi_m, (\mathrm{H}_0 - \alpha_n \mathrm{H}_1)\Phi_n\rangle = 0, \\ \langle(\mathrm{H}_0^T - \alpha_m \mathrm{H}_1^T)\Psi_m, \Phi_n\rangle = \langle\Psi_m, (\mathrm{H}_0 - \alpha_m \mathrm{H}_1)\Phi_n\rangle = 0, \\ (\alpha_n - \alpha_m)\langle\Psi_m, \mathrm{H}_1\Phi_n\rangle = 0. \end{cases} \quad (13)$$

If we have conducted a DNS computation, at a specified location, a vector function $A_0(y)\exp(i\omega t)$ can be obtained by performing a temporal Fourier analysis of the unsteady flow. Combining with the streamwise direction derivative, $\Phi_{DNS} = (A_0, -i\partial A_0/\partial x)^T$, we can find the amplitude of a boundary layer mode as follows:

$$C_\alpha = \frac{\langle\Psi_n, \mathrm{H}_1\Phi_{\mathrm{DNS}}\rangle}{\langle\Psi_n, \mathrm{H}_1\Phi_n\rangle}. \quad (14)$$

The process described above is much simple, and if one has a spatial LST code, it is straightforward to extend it to multimode decomposition. However, it should be noted that such a biorthogonal eigenfunction system is homogeneous, i.e., it is only suitable for a discrete spectrum, but not for a continuous spectrum. Therefore, for the multimode decomposition of the continuous spectrum, the method of Tumin[32] is preferable.

D. Receptivity model

The receptivity of compressible boundary layers to wall perturbations has been solved by Tumin[36] based on the biorthogonal eigenfunction system. Here, a similar receptivity mode is presented below, which is aimed at the receptivity to the spatial distribution of plasma actuation. We consider a general case where the boundary layer is subjected to different types of periodic-in-time and z-direction external disturbances, e.g., sources of mass, momentum, and energy $S(x,y,z,t)$, and inhomogeneous boundary conditions on the wall $\mathbf{u}_w(x,z,t)$ and $T_w(x,z,t)$. In the parallel flow approximation of the two-dimensional flat-plate boundary layer, the external disturbances can be employed; the triple Fourier transform with respect to x, z, and t, and the examples of source and wall blow-suction disturbance are as follows:

$$\hat{S}(\alpha,\beta,\omega,y) = \frac{1}{TZ}\int_0^T dt\int_0^Z dz\int_{-\infty}^{\infty} S(x,y,z,t)e^{-i\alpha x - i\beta z + i\omega t}dx, \quad (15)$$

$$\hat{v}_w(\alpha,\beta,\omega) = \frac{1}{TZ}\int_0^T dt\int_0^Z dz\int_{-\infty}^{\infty} v_w(x,z,t)e^{-i\alpha x - i\beta z + i\omega t}dx, \quad (16)$$

where T and Z indicate the periods of time and the z-direction, respectively. The derivation of the orthogonal relationship between vector $\hat{\phi}$ and adjoint vector $\hat{\varphi}$ is the same with the process described above. The adjoint LST equation can be written in the following form:

$$\mathcal{L}_0^* + \alpha\mathcal{L}_1^*\hat{\varphi} + \alpha^2\mathcal{L}_2^*\hat{\varphi} = 0, \quad (17)$$

where the adjoint operators $\mathcal{L}_0^*$, $\mathcal{L}_1^*$, and $\mathcal{L}_2^*$ are obtained by employing integration by parts and can be found in Appendix B. Imposing a homogeneous boundary condition for the adjoint vector, one can obtain the following orthogonality relation based on the definition of the inner product:

$$\begin{cases} \alpha \neq \alpha_s, \quad \langle\hat{\varphi}_\alpha, [\mathcal{L}_1 + (\alpha+\alpha_s)\mathcal{L}_2]\hat{\phi}_{\alpha_s}\rangle = 0, \\ \alpha = \alpha_s, \quad \langle\hat{\varphi}_\alpha, [\mathcal{L}_1 + (\alpha+\alpha_s)\mathcal{L}_2]\hat{\phi}_{\alpha_s}\rangle = Q. \end{cases} \quad (18)$$

Through solving the spatial Cauchy problem under the assumption of a finite growth rate of the disturbances, Tumin[32] demonstrated that the solution of the linearized disturbance equations can be expanded into the normal modes of continuous and discrete spectra,

$$\begin{aligned} A_0(x,y,\beta,\omega) &= \frac{1}{2\pi}\int_{-\infty}^{\infty}\hat{\phi}_\alpha e^{i\alpha x}d\alpha \\ &= \sum_j\int_0^\infty C_j(k)\hat{\phi}_{\alpha_j(k)}(y,k)e^{i\alpha_j(k)x}dk \\ &\quad + \sum_m C_m\hat{\phi}_{\alpha_m}(y)e^{i\alpha_m x}. \end{aligned} \quad (19)$$

With the help of the above orthogonality relation (18), one can find the amplitude of a mode to the formal solution,

$$Ce^{i\alpha x} = \frac{\langle\hat{\varphi}_\alpha, (\mathcal{L}_1 + 2\alpha\mathcal{L}_2)A_0\rangle}{Q}. \quad (20)$$

Conducting an inner product between $\hat{\varphi}_\alpha$ and the inhomogeneous LST equation, the detailed derivation process of the receptivity coefficients will be given as below, which was missing in the previous paper,

$$\begin{aligned}\langle\hat{\varphi}_\alpha, (\mathcal{L}_0+\alpha_s\mathcal{L}_1+\alpha_s^2\mathcal{L}_2)\hat{\phi}_{\alpha_s}-\hat{S}\rangle\\ &=\langle\hat{\varphi}_\alpha, (\mathcal{L}_0+\alpha\mathcal{L}_1+\alpha^2\mathcal{L}_2)\hat{\phi}_{\alpha_s}\rangle-\langle\hat{\varphi}_\alpha,\hat{S}\rangle+\langle\hat{\varphi}_\alpha,(\alpha_s-\alpha)\\ &\quad\times[\mathcal{L}_1+(\alpha_s+\alpha)\mathcal{L}_2]\hat{\phi}_{\alpha_s}\rangle\\ &=\langle(\mathcal{L}_0^*+\mathcal{L}_1^*+\alpha^2\mathcal{L}_2^*)\hat{\varphi}_\alpha,\hat{\phi}_{\alpha_s}\rangle\\ &\quad+\mathrm{B.C.}-\langle\hat{\varphi}_\alpha,\hat{S}\rangle+\langle\hat{\varphi}_\alpha,(\alpha_s-\alpha)[\mathcal{L}_1+(\alpha_s+\alpha)\mathcal{L}_2]\hat{\phi}_{\alpha_s}\rangle=0.\end{aligned} \tag{21}$$

The first term is equal to zero with the definition of the adjoint equation. The second and third terms represent the forcing from inhomogeneous boundary conditions and sources, respectively. Among them, the explicit expression of the bilinear concomitant B.C. is given in Appendix B.

Based on the orthogonality relation (18) and utilizing (19) and (20), we can arrive at the following identity:

$$Ce^{i\alpha x}=\frac{1}{2\pi Q}\int_{-\infty}^{\infty}\frac{\langle\hat{\varphi}_{\alpha_s},\hat{S}\rangle-\mathrm{B.C.}}{(\alpha_s-\alpha)}e^{i\alpha_s x}d\alpha_s. \tag{22}$$

At this time, we can find the receptivity coefficient as the residue value at the pole $\alpha=\alpha_s$,

$$C=i\frac{\langle\hat{\varphi}_{\alpha_s},\hat{S}\rangle-\mathrm{B.C.}}{Q}. \tag{23}$$

III. TEST CASES AND NUMERICAL SETTING

A. Code validation

Two benchmark cases of a periodic-in-time blowing-suction at supersonic adiabatic flat-plate flows are repeated for the code validation. Those cases have been analyzed by Balakumar and Malik[57] and Tumin.[36] In the first example, the Mach number $Ma_\infty=2.0$ and the dimensionless angular frequency $\omega=0.02$, corresponding to a first mode. In the second example, $Ma_\infty=4.5$ and $\omega=0.2$, corresponding to a Mack mode. The free-stream stagnation temperature of 311 K, the Prandtl number Pr of 0.72, and the Reynolds number $Re_0=1000$ were used for both cases. The shape function $v_w(x, z, \omega)=\delta(x-x_0)\delta(z)$, where v_w is the normal blowing-suction velocity at the wall and δ is Dirac's delta function, so $\hat{v}_w=1$. In addition, the eigenfunction was normalized by the maximum amplitude of the streamwise velocity component. One can see an excellent agreement with Balakumar and Malik[57] in Table I, and it can be considered that the accuracy of the present code in this paper is acceptable.

B. Plasma actuation modeling

A typical surface dielectric barrier discharge (SDBD) actuator is demonstrated in Fig. 1, and the electrodes are supplied with a high voltage power, producing a thin plasma layer over the surface of the plate flat. In terms of plasma and flow interaction, since the plasma generation/propagation time $\tau_p\sim O(\mathrm{ns})\ll\tau_g\sim O(\mu\mathrm{s})$, i.e., the characteristic gas dynamic time, the flow condition affected by the plasma discharge is negligible during a discharge period. Under this assumption, the plasma distribution can be obtained in advance and considered as an input source term of N–S equations, i.e., the computations of plasma dynamics and fluid dynamics are decoupled.

Both volumetric body force and heating source can be produced by plasma actuation. The body force induced by the AC SDBD actuator is usually concerned in subsonic cases, and the accuracy of the empirical model given by Maden *et al.*[58] has been numerically investigated by Dörr and Kloker.[59] However, according to the experimental measurements by Little *et al.*[60] and Roupassov *et al.*,[61] the nanosecond pulsed-DC SDBD actuator transfers very little momentum to the surrounding air, and the actuator-induced gas velocities show near-zero values. In addition, the body force induced by the SDBD actuator is mainly due to the negative ion accumulation inside a volume above the dielectric, whose characteristic time is $O(\mathrm{ms})$. While for the super/hypersonic flow, the flow passing the plasma actuators is so fast that the body force is almost negligible. Therefore, only the heating source is taken into consideration in the present calculations. Recently, an analytical model based on nanosecond pulsed-DC SDBD physics was developed by Soloviev and Krivtsov,[62] which has been validated by in-house plasma dynamics solver PASSKEy,[63] and the expression for the distribution of energy deposition is as follows:

TABLE I. Test cases for LST and receptivity analysis codes.

	Balakumar and Malik[57]		This paper	
β	α	$\lvert C_s\rvert$	α	$\lvert C_s\rvert$
	$Ma_\infty=2.0$, $Re_0=1000$, and $\omega=0.02$			
0	$3.733\times10^{-2}-3.696\times10^{-4}i$	2.2079×10^{-2}	$3.733\times10^{-2}-3.699\times10^{-4}i$	0.0219
0.08	$4.077\times10^{-2}-2.384\times10^{-3}i$	0.2333	$4.077\times10^{-2}-2.384\times10^{-3}i$	0.2335
	$Ma_\infty=4.5$, $Re_0=1000$, and $\omega=0.2$			
0	$0.220-3.091\times10^{-3}i$	1.7537×10^{-2}	$0.220-3.093\times10^{-3}i$	0.0175
0.12	$0.2181+2.969\times10^{-4}i$	1.5405×10^{-2}	$0.2181+2.944\times10^{-4}i$	0.0154

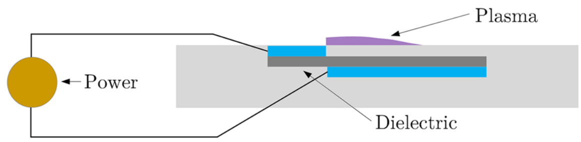

FIG. 1. Schematic illustration of the SDBD plasma actuator.

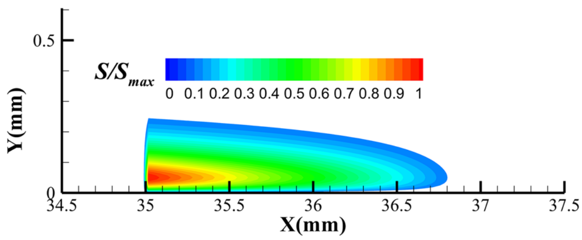

FIG. 2. Distribution of the plasma heating source.

$$S(x,y,t) = S_e(t)S_{max}\left(1 - \frac{x - x_b}{l_s}\right)\frac{y}{h_s}\exp\left(-\frac{y}{h_s}\right), \quad 0 < x - x_b < l_s, \tag{24}$$

where x_b and l_s are the beginning location and streamwise length of the actuation region, respectively. The energy deposition is concentrated in a thin layer near the dielectric surface and coincides with the streamer diameter,[62,63] $h_s \approx 0.05$ mm. $S_{\max}(\mathrm{W/m^3})$ is the characteristic parameter of energy deposition, which depends on the plasma power and dielectric thickness. The distribution of the plasma heating source is illustrated in Fig. 2 as an example. According to the performance of plasma power, the actuation waveform is usually a periodic pulse signal. In the present study, three waveforms are selected to evaluate the robustness of plasma actuation, such as square waves, polynomial waves, and triangular waves. If the plasma actuator is operated at frequency f_s, the function $S_e(t)$ of the square wave is defined as follows:

$$S_e(t) = \begin{cases} 1, & \mathrm{mod}(t, P_s) \le W_s \\ 0, & \mathrm{mod}(t, P_s) \ge W_s, \end{cases} \tag{25}$$

where $P_s = 1/f_s$ and W_s represent the period and pulse width of the signal, respectively, whereas the expression of the polynomial wave is

$$S_e(t) = 20.25\left(\frac{t - t_s}{W_s}\right)^5 - 35.4375\left(\frac{t - t_s}{W_s}\right)^4 + 15.1875\left(\frac{t - t_s}{W_s}\right)^3, \quad t_s \le t \le t_s + W_s, \tag{26}$$

where t_s is the start time of each actuation period. Such a wave shape features a gradual increase and relatively fast drop of the discharge power, which is more consistent with the actual situation. The examples of three different kinds of waveforms in one cycle are shown in Fig. 3.

C. Numerical setting of DNS

In DNS computations, non-uniform grids are employed in both the streamwise and wall-normal directions, and finer grids are clustered in the near-wall region and around the actuation location, as shown in Fig. 4. A buffer region is imposed as the outflow condition downstream so that no waves will be reflected back into the computational domain. In all computational cases, more than 40 grid points are used within one wavelength. In addition, since the pulse width of actuation is only tens of nanoseconds, the time step of 5 ns is adopted in the explicit time advancing. Both grid and time step refinement studies have been conducted to guarantee the convergence of numerical simulation results based on the above setting. For each DNS case presented below, the unsteady computations are carried out until the flow field reaches a periodic state. After that, a temporal Fourier analysis is conducted on the results of the unsteady flow to obtain the disturbance amplitudes of specific frequency.

IV. RESULTS AND DISCUSSION

The freestream conditions used by Ma and Zhong[22] are considered in the present research, i.e., a Mach 4.5 boundary layer flow over an adiabatic flat plate in which the instability Mack mode is dominant. The temperature is $T_\infty = 65.15$ K, and the unit Reynolds number is $Re_\infty = 7.2 \times 10^6\ \mathrm{m^{-1}}$.

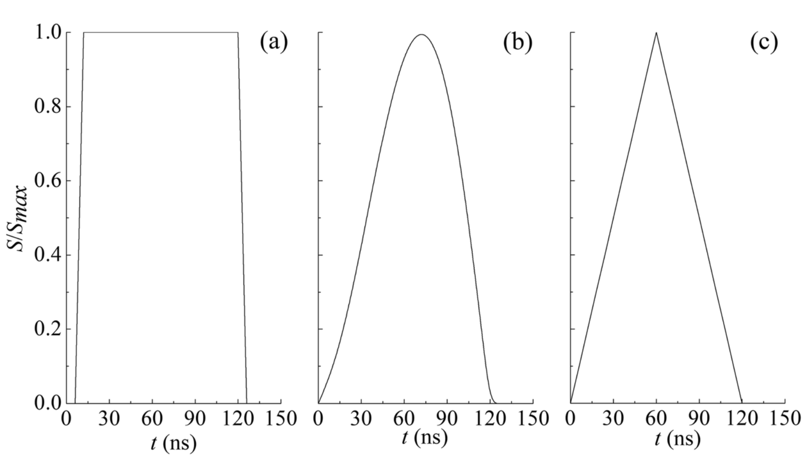

FIG. 3. Three kinds of wave shapes: (a) square wave, (b) polynomial wave, and (c) triangular wave.

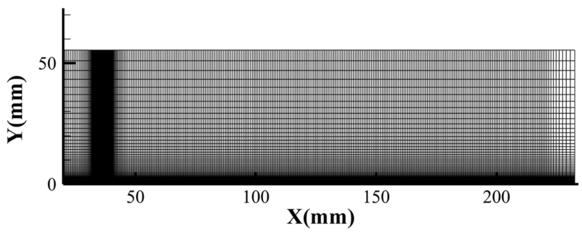

FIG. 4. Computational grid, every five grid points are displayed.

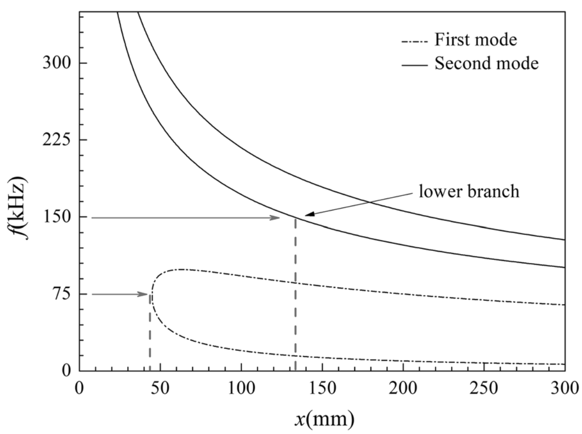

FIG. 5. Neutral curves of the two-dimensional disturbances.

A. Discrete modes

The characteristic of the discrete spectrum of the high-speed boundary has been thoroughly studied by Ma and Zhong[22] and Fedorov and Tumin.[19] Nevertheless, before studying the receptivity of plasma actuation, a brief introduction to this problem should be presented for the sake of research completeness. The neutral curves of the two-dimensional ($\beta = 0$) disturbance are shown in Fig. 5. It can be seen that the disturbances at $f = 75$ kHz and $f = 150$ kHz are corresponding to the typical first and second modes, respectively. The evolutions of the fast and slow discrete modes at two different frequencies are presented in Fig. 6. Under such a flow condition, the slow modes become unstable first and second modes once passing through the lower branch of the neutral curve. For the discrete spectrum at $f = 150$ kHz, there is a synchronization between slow and fast modes, while the synchronization point of $f = 75$ kHz is much more downstream, not been seen within this scope.

We consider a single fast mode imposing at the start location $x = 70$ mm, and the amplitude of the maximum streamwise velocity is 2×10^{-5}, which is small enough to preserve the linear properties of the disturbance. The amplitude of the disturbance along the downstream computed by DNS is shown in Fig. 7(a), and the multimode decomposition to fast and slow modes, as well as linear parabolized stability equation (LPSE) results, is also shown for comparison. Even though there is no slow mode at the start location, the slow mode with a small amplitude still appears in the flow field due to the scattering effect of non-parallel mean-flow. Then, the slow mode converts to the unstable second mode after synchronizing with the fast mode.

When the incoming wave is composed of both slow and fast modes having the same amplitude (2×10^{-5}) and frequency ($f = 150$ kHz), the evolution of such disturbances is presented in Fig. 7(b). One can see that there is a long-period oscillation before the instability mode dominates. Such a phenomenon is due to the coexistence of two discrete modes in the boundary layer, i.e., the "beat" effect, which can be simply interpreted by converting summation to multiplication of two trigonometric functions with the same period. In addition, a LPSE calculation of the slow and fast modes is also shown, and the amplitude is slightly smaller than that of DNS. The above results confirm the scenario suggested by Fedorov and Khokhlov.[17] Since the decaying mode can give rise to the unstable mode, which may lead to the transition, both the slow and fast discrete modes should be considered in the laminar–turbulent transition. These features of the fast and slow discrete modes of high-speed boundary layers motivate the research on the receptivity of

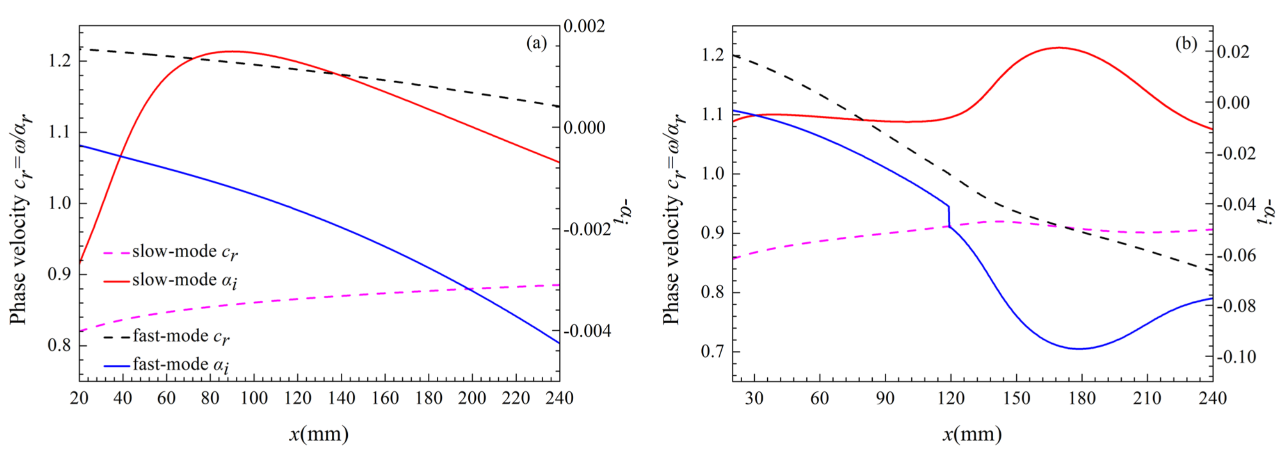

FIG. 6. Evolution of the discrete spectrum of perturbations at (a) $f = 75$ kHz and (b) $f = 150$ kHz.

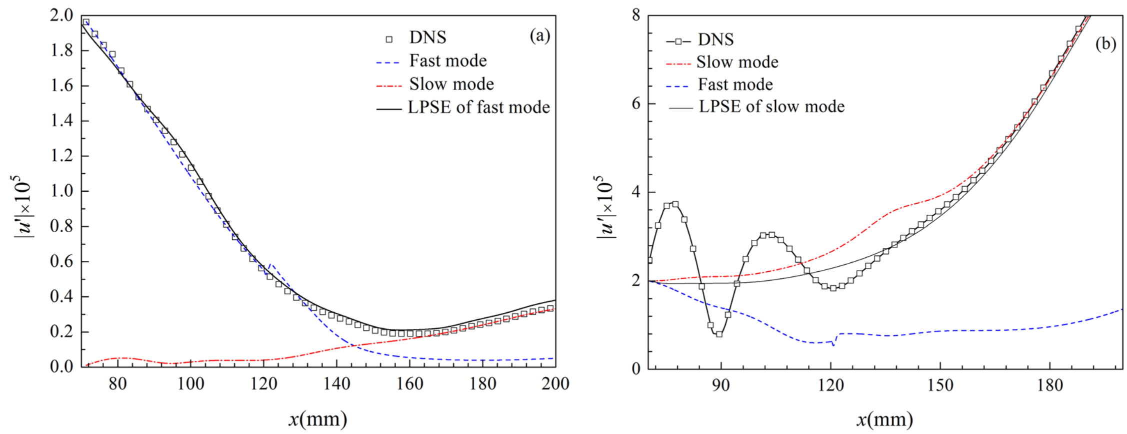

FIG. 7. Evolutions of the disturbance amplitude with different inflow boundary conditions: (a) a single fast mode and (b) the combination of fast and slow modes.

TABLE II. Parameters of numerical simulations performed.

Case	Shape	x_b (mm)	l_s (mm)	f_s (kHz)	W_s (ns)
S1F1	Square	35	2.0	150	120
S1W1	Square	35	2.0	150	60
T1F1	Triangular	35	2.0	150	120
P1F1	Polynomial	35	2.0	150	120
S1F2	Square	35	2.0	75	120

the decaying mode to the external perturbations, which is important in different flow control strategies.

B. Response to plasma actuation

The receptivity of the supersonic boundary layer to the periodic two-dimensional plasma actuation is discussed in this section. For the plasma actuator, there are five variable parameters by manipulating the plasma power, i.e., waveform, frequency, period, and width of the actuation signal, as well as the streamwise length of the actuation region. Five typical cases with different variable parameters are selected, and the detailed information is presented in Table II. To study the effect of actuator parameters on the receptivity coefficient, we keep the total discharge power P_t(W/m) constant if there is no special statement. Such consideration is preferable in practical applications because the total power is much easier to control than the other actuator parameters. The total power P_t can be computed as

$$P_t = \left(\int_0^{W_s} dt \int_{x_b}^{x_b+l_s} dx \int_0^{\infty} S(x,y,t)dy\right) \times f_s = \text{constant}. \quad (27)$$

To show the overall feature of the unsteady flow field, Fig. 8 shows the contours of instantaneous pressure and temperature fluctuations induced by the plasma actuation in case S1F1 in which the total power is equal to 2 W/m. Downstream of the actuation region,

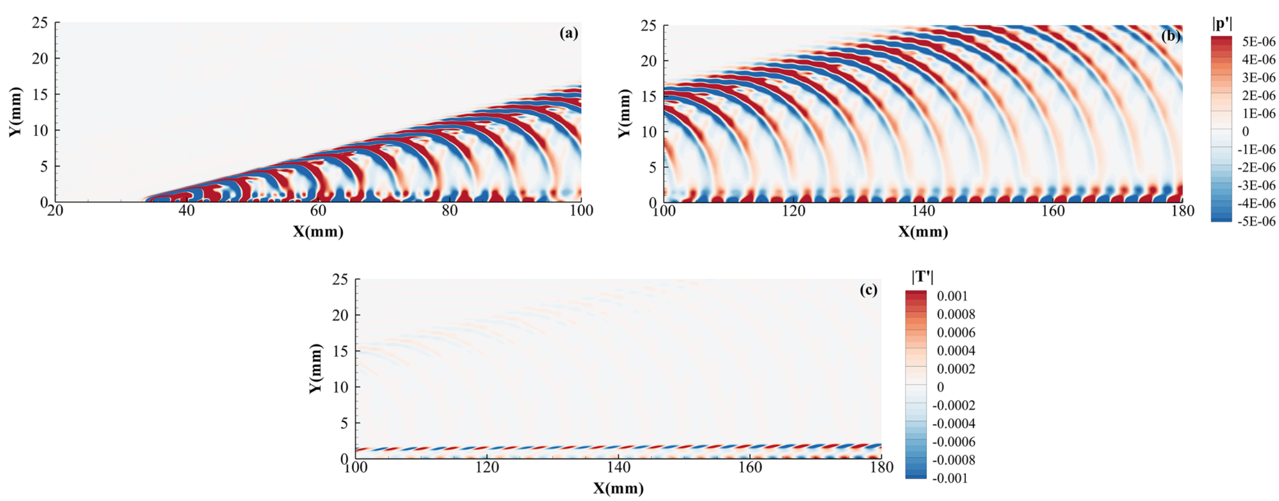

FIG. 8. Contours of instantaneous pressure [(a) and (b)] and temperature (c) fluctuation induced plasma actuation of case SIF1.

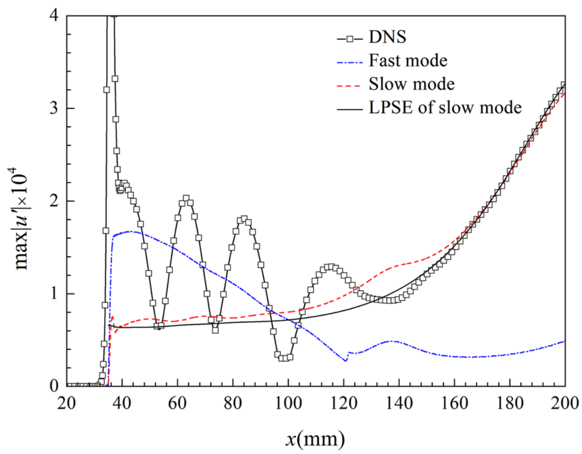

FIG. 9. Evolution of the maximum streamwise disturbance velocity of f_s = 150 kHz in case S1F1.

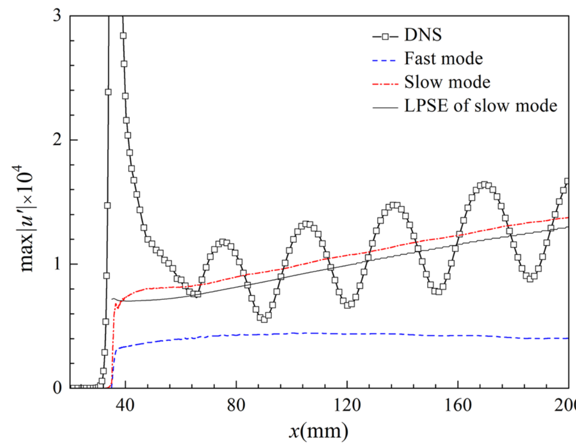

FIG. 11. Evolution of the maximum streamwise disturbance velocity of f_s = 75 kHz in case S1F2.

the excited pressure fluctuations are divided into two branches. One branch penetrates the external flow outside the boundary layer and propagates along the Mach lines, i.e., the acoustic wave of the continuous spectrum, which decays downstream due to its inherent stable property, while the other branch stays within the boundary layer, i.e., discrete modes. Such boundary layer modes grow substantially after passing the lower neutral branch and become the dominant second mode, which is indicated by the typical wave structures inside the boundary layer. Similar behaviors of the disturbance field can be observed in the other four cases.

Figure 9 illustrates the evolution of maximum streamwise disturbance velocity at f_s = 150 kHz of case S1F1, and the results by the multimode decomposition of DNS to fast and slow modes are presented as well. It can be seen that both the fast and slow modes can be excited by plasma actuation, and the amplitude of the fast mode is much higher than that of the slow mode. The result of the LPSE computation of the slow mode started with the amplitude obtained from the multimode decomposition is presented as well. Downstream of the actuation region, a "beat" structure appears, and the slow mode becomes dominant after synchronization with the fast mode. Figure 10 shows good agreement between eigenfunctions of the slow mode and the disturbance profiles obtained from DNS at x = 180 mm.

If we change the waveform or width of the actuation signal in cases S1W1, T1F1, and P1F1, but keep the total power constant, interestingly, the evolutions of disturbances in those cases are the same as that of case S1F1. In case S1F2, the plasma actuation at the frequency of f_s = 75 kHz is imposed. Figure 11 shows the disturbance evolutions of f_s = 75 kHz computed by DNS and also includes the multimode decomposition results. In addition, the result of the LPSE computation started with the amplitude obtained from the

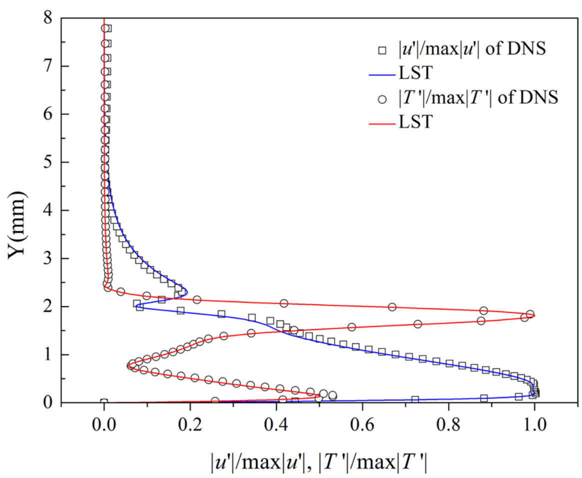

FIG. 10. Comparison of the eigenfunctions of the slow mode with DNS at x = 180 mm in case S1F1.

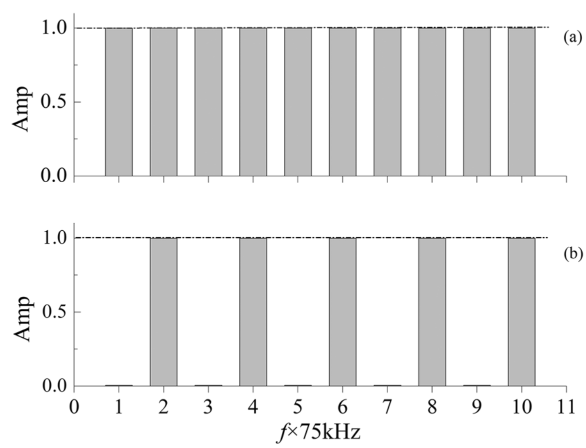

FIG. 12. Fourier components of 75 kHz multiplication in (a) case S1F2 and (b) cases S1F1, S1W1, T1F1, and P1F1.

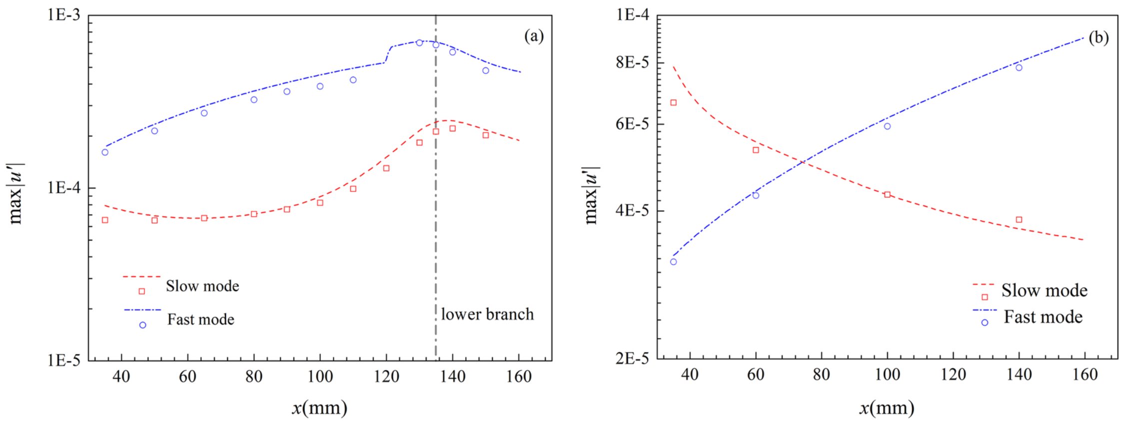

FIG. 13. Receptivity coefficients of plasma actuation at different streamwise locations: (a) f_s = 150 kHz and (b) f_s = 75 kHz. Theoretical results are denoted by lines, and DNS results are denoted by symbols.

multimode decomposition is presented as well. According to the discrete spectrum of f = 75 kHz in Fig. 6, there is no synchronization between fast and slow modes, and so the co-existence of two modes can hold for a long distance. However, the disturbance amplitude of f_s = 150 kHz in this case is also consistent with that of case S1F1. This phenomenon can be interpreted by temporal Fourier analysis of the function $S_e(t)$. Because the plasma actuation signal is a typical periodic pulse signal, the Fourier components with multiples of actuation frequency can be excited effectively. The amplitude coefficients of different frequency components are presented in Fig. 12, and their amplitudes have been normalized to unity by the same value for ease of comparison. It can be seen that the signal amplitude of 150 kHz is the same in all cases described above, and so the same disturbance evolution of the corresponding frequency is expected. It should be noted that the disturbance of f = 300 kHz is also excited, while it decays quickly downstream according to the neutral curve in Fig. 5; as a result, only the f = 150 kHz instability mode dominates in far downstream. In other words, even though only low-frequency actuations are imposed, the high-frequency disturbances can be effectively excited in the boundary layer, which is qualitatively consistent with the experimental results of Li and Zhang[64] and Li *et al.*[65] In their experiments, the glow discharge was introduced as an artificial disturbance, whose discharge characteristics are essentially consistent with the SDBD actuator considered in the present study. Their experimental results demonstrate that even though only the artificial disturbance in the first mode frequency range is introduced, the other modes of frequency multiplication can be excited as well. Among them, the Mack mode with the highest growth rate becomes the dominant one in the boundary layer.

C. Parameters research of receptivity coefficients

In this section, theoretical analysis and many cases of DNS computation are conducted to investigate the effect of the streamwise location and the width of the actuator on the receptivity coefficients. Figures 13(a) and 13(b) show the maximum streamwise disturbance velocity of fast and slow modes excited by plasma actuations at different streamwise locations. Consistent with the study above, two typical actuation frequencies of 150 kHz and 75 kHz are considered here, which correspond to the first and second modes, respectively. In all cases of Figs. 13(a) and 13(b), the streamwise width of the actuation region is 2 mm, and the total power is maintained at 2 W/m. With the help of the multimode decomposition, the amplitudes of discrete modes are filtered out from the DNS computations at the center of the actuation region. One can see that amplitudes predicted by the receptivity model reach good agreement with those of numerical calculations at both 150 kHz and 75 kHz.

For the plasma actuation of 75 kHz, the receptivity coefficients of the slow mode decrease when the actuator shifts from upstream to downstream, whereas the fast mode shows the opposite trend. For the actuation frequency of 150 kHz, the receptivity coefficients

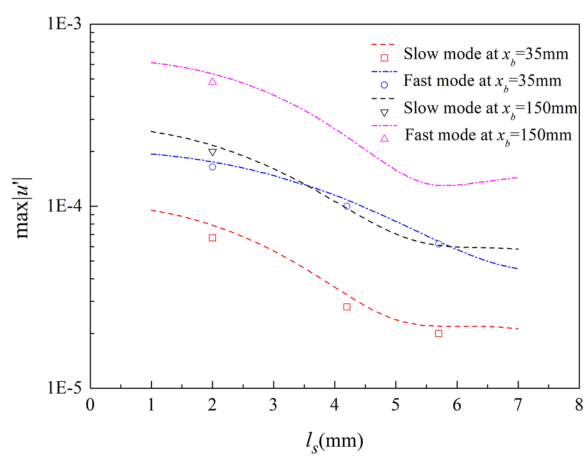

FIG. 14. Receptivity coefficients of plasma actuation with different streamwise widths at two different streamwise locations x_b = 35 mm and x_b = 150 mm. Theoretical results are denoted by lines, and DNS results are denoted by symbols.

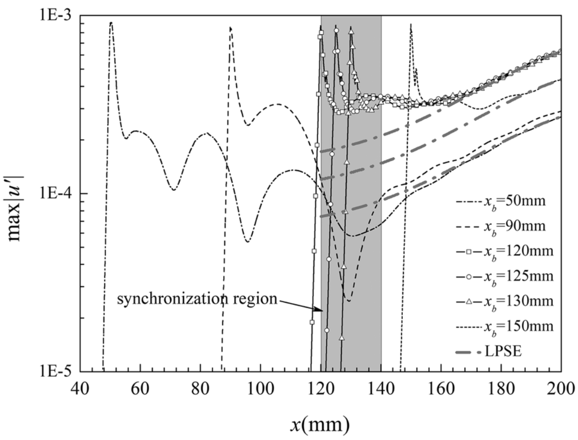

FIG. 15. Evolution of maximum streamwise at the disturbance velocity of f_s = 150 kHz excited by plasma actuation at different streamwise locations.

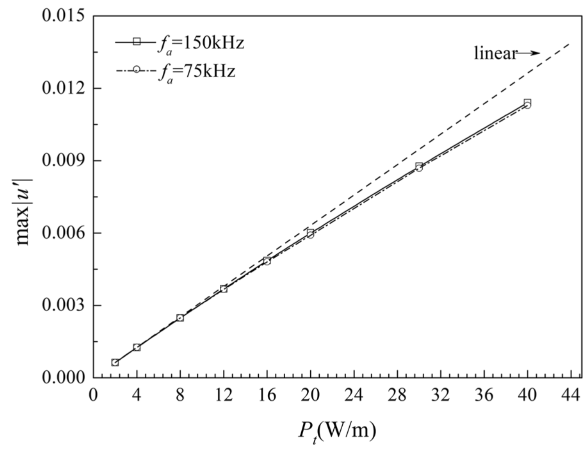

FIG. 17. The disturbance amplitude of f_s = 75 kHz and f_s = 150 kHz at x = 200 mm excited plasma actuation with increasing total power.

of the fast mode also increase gradually with the actuation moving toward the synchronization point but decrease at the downstream of the lower branch of neutral curve, where the slow mode is synchronized with the fast mode. The slow mode only decreases slightly near the leading-edge region, and the behavior of downstream is similar to that of the fast mode. Such an effect of the region location on the receptivity coefficients is consistent with the research results of wall blowing-suction perturbation, which were obtained by Tumin *et al.*[34] and Wang *et al.*[30]

When the location and total power of the actuation remain unchanged, the effect of the streamwise length of the actuation region on the receptivity coefficients is presented in Fig. 14. When the actuation is located upstream or downstream of the synchronization point, the receptivity coefficients both decrease with a longer actuation region.

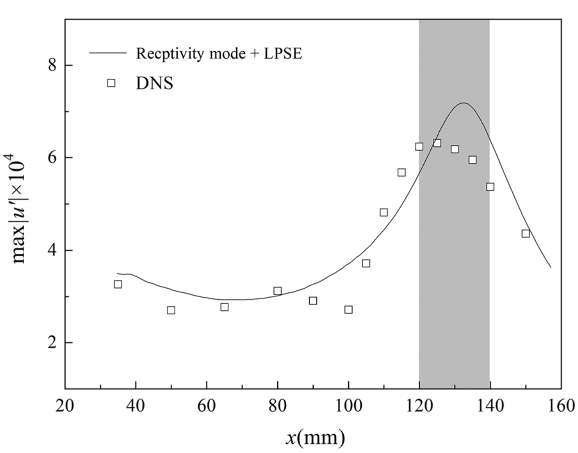

FIG. 16. A comparison between the theoretical method and DNS for the disturbance amplitude at x = 200 mm excited by plasma actuation at different streamwise locations.

For practical transition control technology, the excited disturbance amplitude at the downstream of the actuation region is much more concerned, which can explicitly reflect the efficiency of the actuator. Figure 15 illustrates the evolution of the maximum streamwise disturbance velocity excited by the plasma actuation of f_s = 150 kHz at six different locations, and even though the instantaneous flow field near the actuation is complex, the instability boundary mode becomes dominant far downstream from the lower neutral branch, whose growth rates can be obtained by LPSE computations. One can note that when the actuator is located near the synchronization point, the disturbance amplitudes are almost equal. For the sake of comparison, the disturbance amplitudes at x = 200 mm excited by plasma actuation at different streamwise locations are plotted in Fig. 16. We consider a theoretical prediction method by the combination of receptivity model and LPSE, i.e., the amplitude of the slow mode predicted by the receptivity mode is used as the initial value of LPSE computation, and the disturbance growth downstream can be obtained. The results computed by such a method are presented in Fig. 16. It can be seen that the agreement between the theoretical method and DNS near the synchronization point or lower neutral branch is not as good. As discussed by Fedorov and Khokhlov,[17] there is an intermodal exchange near the synchronization point, which results in that the normal mode decomposition is not valid. This means that the non-parallel effect and multimode characteristic have to be considered near this region.

When the actuator parameters are set as the same as case S1F2, increasing the total power, the excited disturbance amplitudes at x = 200 mm are presented in Fig. 17. The linear receptivity process is also validated even when the total power reaches up to 40 W/m, and a receptivity efficiency function of $\Lambda = |u'|/P_t$ can be obtained, which plays a useful guiding role in engineering applications.

V. CONCLUSIONS

In this paper, the receptivity of a Mach 4.5 flat-plate boundary layer to plasma heating source actuation has been studied by

DNS and stability analysis. The objective of the current research is to evaluate the receptivity of the pulsed-DC SDBD plasma actuator as a novel flow control technology for the boundary layer transition. The main conclusions of the current research are as follows:

(1) Because the plasma actuation is typical periodic pulse signals, when the total power remains constant, the Fourier components with multiples of the actuation frequency have the same energy, regardless of the waveform, period, and width of the actuation signal. As a result, the same response of the boundary layer to plasma actuation at the corresponding frequency is expected. Such characteristics benefit the robustness of the plasma actuator. In addition, the above research findings can be used to qualitatively explain the experimental results of Li and Zhang[64] and Li *et al.*[65]

(2) Inspired by Tumin,[31–33] a simple scheme of biorthogonal multimode decomposition is developed. With the help of the multimode decomposition technique, the amplitude of concerned discrete modes can be obtained. The numerical results demonstrate that both fast and slow modes can be excited by plasma actuation. The effect of the actuation streamwise location on the receptivity coefficients is similar to wall blowing-suction perturbation,[30,34] and the receptivity maximum is observed near the lower neutral branch, where the slow mode is synchronized with the fast mode. In addition, if maintaining the total power fixed, the receptivity coefficients decrease with a longer actuation region. The above results of parameter research may provide better plasma actuator strategies.

(3) A theoretical prediction method by the combination of the receptivity model and LPSE is considered in the present study. A good agreement with the DNS results is reached, except near the synchronization point in which the nonparallel effect and multimode interaction[17,27] can no longer be neglected. Nevertheless, such a rapid theoretical prediction is acceptable in practical engineering applications, and feedback control can be conducted by manipulating plasma power supply. Besides, only the results of the two-dimensional actuation ($\beta = 0$) are presented in this paper, but a similar behavior of receptivity can be obtained with the three-dimensional actuation.

ACKNOWLEDGMENTS

This work was funded by the National Key Research and Development Program of China (Grant No. 2016YFA0401200), the Natural Science Foundation of China (Grant Nos. 51776222, 11772316, and 51907205), and the Basic Research Program of Natural Science of Shaanxi Province (Grant No. 2018JQ1011).

APPENDIX A: NONZERO ELEMENTS OF THE OPERATORS IN EQ. (4)

$$\Gamma_{11} = 1.0, \quad \Gamma_{22} = \bar{\rho}, \quad \Gamma_{33} = \bar{\rho}, \quad \Gamma_{44} = \bar{\rho}, \quad \Gamma_{51} = \frac{1-\gamma}{\gamma}\bar{T}, \quad \Gamma_{55} = \frac{\bar{\rho}}{\gamma},$$

$$A_{11} = \bar{u}, \quad A_{12} = \bar{\rho},$$

$$A_{21} = \frac{\bar{T}}{\gamma Ma^2}, \quad A_{22} = \bar{\rho}\bar{u} - \frac{4}{3}\frac{1}{Re_0}\frac{\partial\bar{\mu}}{\partial x}, \quad A_{23} = -\frac{1}{Re_0}\frac{\partial\bar{\mu}}{\partial y},$$

$$A_{25} = \frac{\bar{\rho}}{\gamma Ma^2} - \frac{1}{Re_0}\frac{\partial\bar{\mu}}{\partial\bar{T}}\left(\frac{4}{3}\frac{\partial\bar{u}}{\partial x} - \frac{2}{3}\frac{\partial\bar{v}}{\partial y}\right),$$

$$A_{32} = \frac{2}{3}\frac{1}{Re_0}\frac{\partial\bar{\mu}}{\partial y}, \quad A_{33} = \bar{\rho}\bar{u} - \frac{1}{Re_0}\frac{\partial\bar{\mu}}{\partial x}, \quad A_{35} = -\frac{1}{Re_0}\frac{d\bar{\mu}}{d\bar{T}}\left(\frac{\partial\bar{u}}{\partial y} + \frac{\partial\bar{v}}{\partial x}\right),$$

$$A_{44} = \bar{\rho}\bar{u} - \frac{1}{Re_0}\frac{\partial\bar{\mu}}{\partial x}, \quad A_{51} = \frac{1-\gamma}{\gamma}\bar{T}\bar{u},$$

$$A_{52} = \frac{(1-\gamma)Ma^2\bar{\mu}}{Re_0}\left(\frac{8}{3}\frac{\partial\bar{u}}{\partial x} - \frac{4}{3}\frac{\partial\bar{v}}{\partial y}\right), \quad A_{53} = \frac{2(1-\gamma)Ma^2\bar{\mu}}{Re_0}\left(\frac{\partial\bar{v}}{\partial x} + \frac{\partial\bar{u}}{\partial y}\right),$$

$$A_{55} = \frac{\bar{\rho}\bar{u}}{\gamma} - \frac{1}{\mathrm{Re}_0 Pr}\left(\frac{\partial\bar{\mu}}{\partial x} + \frac{d\bar{\mu}}{\partial\bar{T}}\frac{\partial\bar{T}}{\partial x}\right);$$

$$B_{11} = \bar{v}, \quad B_{13} = \bar{\rho},$$

$$B_{22} = \bar{\rho}\bar{v} - \frac{1}{Re_0}\frac{\partial\bar{\mu}}{\partial y}, \quad B_{23} = \frac{2}{3}\frac{1}{Re_0}\frac{\partial\bar{\mu}}{\partial x}, \quad B_{25} = -\frac{1}{Re_0}\frac{\partial\bar{\mu}}{\partial\bar{T}}\left(\frac{\partial\bar{u}}{\partial y} + \frac{\partial\bar{v}}{\partial x}\right),$$

$$B_{31} = \frac{\bar{T}}{\gamma Ma^2}, \quad B_{32} = -\frac{1}{Re_0}\frac{\partial\bar{\mu}}{\partial x}, \quad B_{33} = \bar{\rho}\bar{v} - \frac{4}{3}\frac{1}{Re_0}\frac{\partial\bar{\mu}}{\partial y},$$

$$B_{35} = \frac{\bar{\rho}}{\gamma Ma^2} - \frac{1}{Re_0}\frac{d\bar{\mu}}{d\bar{T}}\left(-\frac{2}{3}\frac{\partial\bar{u}}{\partial x} + \frac{4}{3}\frac{\partial\bar{v}}{\partial y}\right),$$

$$B_{44} = \bar{\rho}\bar{v} - \frac{1}{Re_0}\frac{\partial\bar{\mu}}{\partial y}, \quad B_{51} = \frac{1-\gamma}{\gamma}\bar{T}\bar{v}, \quad B_{52} = \frac{2(1-\gamma)Ma^2\bar{\mu}}{Re_0}\left(\frac{\partial\bar{u}}{\partial y} + \frac{\partial\bar{v}}{\partial x}\right),$$

$$B_{53} = \frac{(1-\gamma)Ma^2\bar{\mu}}{Re_0}\left(\frac{8}{3}\frac{\partial\bar{v}}{\partial y} - \frac{4}{3}\frac{\partial\bar{u}}{\partial x}\right), \quad B_{55} = \frac{\bar{\rho}\bar{v}}{\gamma} - \frac{1}{Re_0 Pr}\left(\frac{\partial\bar{\mu}}{\partial y} + \frac{d\bar{\mu}}{d\bar{T}}\frac{\partial\bar{T}}{\partial y}\right);$$

$$C_{14} = \bar{\rho}, \quad C_{24} = \frac{2}{3}\frac{1}{Re_0}\frac{\partial\bar{\mu}}{\partial x}, \quad C_{34} = \frac{2}{3}\frac{1}{Re_0}\frac{\partial\bar{\mu}}{\partial y},$$

$$C_{41} = \frac{\bar{T}}{\gamma Ma^2}, \quad C_{42} = -\frac{1}{Re_0}\frac{\partial\bar{\mu}}{\partial x}, \quad C_{43} = -\frac{1}{Re_0}\frac{\partial\bar{\mu}}{\partial y},$$

$$C_{45} = \frac{\bar{\rho}}{\gamma Ma^2} - \frac{1}{Re_0}\frac{d\bar{\mu}}{d\bar{T}}\left(-\frac{2}{3}\frac{\partial\bar{u}}{\partial x} - \frac{2}{3}\frac{\partial\bar{v}}{\partial y}\right),$$

$$C_{54} = \frac{(1-\gamma)Ma^2\bar{\mu}}{Re_0}\left(-\frac{4}{3}\frac{\partial\bar{u}}{\partial x} - \frac{4}{3}\frac{\partial\bar{v}}{\partial y}\right);$$

$$D_{11} = \frac{\partial\bar{u}}{\partial x} + \frac{\partial\bar{v}}{\partial y}, \quad D_{12} = \frac{\partial\bar{\rho}}{\partial x}, \quad D_{13} = \frac{\partial\bar{\rho}}{\partial y},$$

$$D_{21} = \bar{u}\frac{\partial \bar{u}}{\partial x} + \bar{v}\frac{\partial \bar{u}}{\partial y} + \frac{1}{\gamma Ma^2}\frac{\partial \bar{T}}{\partial x}, \quad D_{22} = \bar{\rho}\frac{\partial \bar{u}}{\partial x}, \quad D_{23} = \bar{\rho}\frac{\partial \bar{u}}{\partial y},$$

$$D_{25} = \frac{1}{\gamma Ma^2}\frac{\partial \bar{p}}{\partial x} - \frac{1}{Re_0}\frac{\partial}{\partial x}\left(\frac{d\bar{\mu}}{d\bar{T}}\right)\left(\frac{4}{3}\frac{\partial \bar{u}}{\partial x} - \frac{2}{3}\frac{\partial \bar{v}}{\partial y}\right) - \frac{1}{Re_0}\frac{\partial}{\partial y}\left(\frac{d\bar{\mu}}{d\bar{T}}\right) \times \left(\frac{\partial \bar{u}}{\partial y} + \frac{\partial \bar{v}}{\partial x}\right) - \frac{1}{Re_0}\frac{d\bar{\mu}}{d\bar{T}}\left(\frac{4}{3}\frac{\partial^2 \bar{u}}{\partial x^2} + \frac{\partial^2 \bar{u}}{\partial y^2} + \frac{1}{3}\frac{\partial^2 \bar{v}}{\partial x \partial y}\right),$$

$$D_{31} = \bar{u}\frac{\partial \bar{v}}{\partial x} + \bar{v}\frac{\partial \bar{v}}{\partial y} + \frac{1}{\gamma Ma^2}\frac{\partial \bar{T}}{\partial y}, \quad D_{32} = \bar{\rho}\frac{\partial \bar{v}}{\partial x}, \quad D_{33} = \bar{\rho}\frac{\partial \bar{v}}{\partial y},$$

$$D_{35} = \frac{1}{\gamma Ma^2}\frac{\partial \bar{p}}{\partial y} - \frac{1}{Re_0}\frac{\partial}{\partial x}\left(\frac{d\bar{\mu}}{d\bar{T}}\right)\left(\frac{\partial \bar{u}}{\partial y} + \frac{\partial \bar{v}}{\partial x}\right) - \frac{1}{Re_0}\frac{\partial}{\partial y}\left(\frac{d\bar{\mu}}{d\bar{T}}\right) \times \left(-\frac{2}{3}\frac{\partial \bar{u}}{\partial x} + \frac{4}{3}\frac{\partial \bar{v}}{\partial y}\right) - \frac{1}{Re_0}\frac{d\bar{\mu}}{d\bar{T}}\left(\frac{4}{3}\frac{\partial^2 \bar{v}}{\partial y^2} + \frac{\partial^2 \bar{v}}{\partial x^2} + \frac{1}{3}\frac{\partial^2 \bar{u}}{\partial x \partial y}\right),$$

$$D_{51} = \frac{\bar{u}}{\gamma}\frac{\partial \bar{T}}{\partial x} + \frac{\bar{v}}{\gamma}\frac{\partial \bar{T}}{\partial y}, \quad D_{52} = \frac{\bar{\rho}}{\gamma}\frac{\partial \bar{T}}{\partial x} + \frac{1-\gamma}{\gamma}\bar{T}\frac{\partial \bar{p}}{\partial x},$$

$$D_{53} = \frac{\bar{\rho}}{\gamma}\frac{\partial \bar{T}}{\partial y} + \frac{1-\gamma}{\gamma}\bar{T}\frac{\partial \bar{p}}{\partial y}, \quad D_{55} = \frac{1-\gamma}{\gamma}\left(\bar{u}\frac{\partial \bar{p}}{\partial x} + \bar{v}\frac{\partial \bar{p}}{\partial y}\right),$$

$$D_{55} = \frac{1-\gamma}{\gamma}\left(\bar{u}\frac{\partial \bar{p}}{\partial x} + \bar{v}\frac{\partial \bar{p}}{\partial y}\right) - \frac{1}{Re_0 Pr}\left(\frac{\partial}{\partial x}\left(\frac{d\bar{\mu}}{d\bar{T}}\right)\frac{\partial \bar{T}}{\partial x} + \frac{\partial}{\partial y}\left(\frac{d\bar{\mu}}{d\bar{T}}\right)\frac{\partial \bar{T}}{\partial y} + \frac{d\bar{\mu}}{d\bar{T}}\frac{\partial^2 \bar{T}}{\partial x^2} + \frac{d\bar{\mu}}{d\bar{T}}\frac{\partial^2 \bar{T}}{\partial y^2}\right) - \frac{(\gamma-1)Ma^2}{Re_0} \times \frac{d\bar{\mu}}{d\bar{T}}\left[\frac{4}{3}\left(\frac{\partial \bar{u}}{\partial x}\right)^2 + \frac{4}{3}\left(\frac{\partial \bar{v}}{\partial y}\right)^2 - \frac{4}{3}\frac{\partial \bar{u}}{\partial x}\frac{\partial \bar{v}}{\partial y} + \left(\frac{\partial \bar{u}}{\partial y} + \frac{\partial \bar{v}}{\partial x}\right)^2\right];$$

$$V_{22}^{xx} = \frac{4}{3}\frac{\bar{\mu}}{Re_0}, \quad V_{33}^{xx} = V_{44}^{xx} = \frac{\bar{\mu}}{Re_0}, \quad V_{55}^{xx} = \frac{\bar{\mu}}{Re_0 Pr};$$

$$V_{22}^{yy} = \frac{\bar{\mu}}{Re_0}, \quad V_{33}^{yy} = \frac{4}{3}\frac{\bar{\mu}}{Re_0}, \quad V_{44}^{yy} = \frac{\bar{\mu}}{Re_0}, \quad V_{55}^{yy} = \frac{\bar{\mu}}{Re_0 Pr};$$

$$V_{22}^{zz} = \frac{\bar{\mu}}{Re_0}, \quad V_{33}^{zz} = \frac{\bar{\mu}}{Re_0}, \quad V_{44}^{zz} = \frac{4}{3}\frac{\bar{\mu}}{Re_0}, \quad V_{55}^{zz} = \frac{\bar{\mu}}{Re_0 Pr};$$

$$V_{23}^{xy} = V_{32}^{xy} = \frac{1}{3}\frac{\bar{\mu}}{Re_0};$$

$$V_{24}^{xz} = V_{42}^{xz} = \frac{1}{3}\frac{\bar{\mu}}{Re_0};$$

$$V_{34}^{yz} = V_{43}^{yz} = \frac{1}{3}\frac{\bar{\mu}}{Re_0}.$$

APPENDIX B: THE BIORTHOGONAL EIGENFUNCTION SYSTEM

In Sec. II, the LST operator is expressed as

$$\mathcal{L}_0 + \alpha\mathcal{L}_1\hat{\phi} + \alpha^2\mathcal{L}_2\hat{\phi} = 0,$$

where

$$\mathcal{L}_0 = D + i\beta C - i\omega\Gamma + \beta^2 V_{zz} + (B - i\beta V_{yz})\frac{\partial}{\partial y} - V_{yy}\frac{\partial^2}{\partial y^2},$$

$$\mathcal{L}_1 = iA + \beta V_{xz} - iV_{xy}\frac{\partial}{\partial y}, \quad \text{and} \quad \mathcal{L}_2 = V_{xx}.$$

The adjoint operator and bilinear concomitant B.C. can be obtained by performing integration by parts,

$$\mathcal{L}_0^* + \alpha\mathcal{L}_1^*\hat{\varphi} + \alpha^2\mathcal{L}_2^*\hat{\varphi} = 0,$$

where

$$\mathcal{L}_0^* = D^T + i\beta C^T - i\omega\Gamma^T + \beta^2 V_{zz}^T - \frac{\partial(B - i\beta V_{yz})^T}{\partial y} - \frac{\partial^2 V_{yy}^T}{\partial y^2} - \left(B^T - i\beta\frac{\partial V_{yz}^T}{\partial y} + 2\frac{\partial V_{yy}^T}{\partial y}\right)\frac{\partial}{\partial y} - V_{yy}^T\frac{\partial^2}{\partial y^2},$$

$$\mathcal{L}_1^* = iA^T + \beta V_{xz}^T + i\frac{\partial V_{xy}^T}{\partial y} + iV_{xy}^T\frac{\partial}{\partial y}, \quad \text{and} \quad \mathcal{L}_2^* = V_{xx}^T.$$

Taking into account the explicit forms of the LST operator and the homogeneous boundary conditions of the adjoint equation, the B.C. can be derived as follows:

$$\text{B.C.} = \bar{\rho}_w\hat{\rho}_w^*\hat{v}_w + \frac{\bar{\mu}}{Re_0}\frac{\partial \hat{u}_w^*}{\partial y}\hat{u}_w + \frac{3\bar{\mu}}{4Re_0}\frac{\partial \hat{v}_w^*}{\partial y}\hat{v}_w + \frac{\bar{\mu}}{Re_0}\frac{\partial \hat{w}_w^*}{\partial y}\hat{w}_w + \frac{\bar{\mu}}{Re_0 Pr}\frac{\partial \hat{T}_w^*}{\partial y}\hat{T}_w,$$

where the superscript $*$ and subscript w indicate the adjoint eigenfunctions and the variables at the wall, respectively.

DATA AVAILABILITY

The data that support the findings of this study are available from the corresponding author upon reasonable request.

REFERENCES

[1] A. Fedorov, "Transition and stability of high-speed boundary layers," Annu. Rev. Fluid Mech. **43**, 79–95 (2011).
[2] X. Zhong and X. Wang, "Direct numerical simulation on the receptivity, instability, and transition of hypersonic boundary layers," Annu. Rev. Fluid Mech. **44**, 527–561 (2012).
[3] C. Lee and S. Chen, "Recent progress in the study of transition in hypersonic boundary layer," Natl. Sci. Rev. **6**, 155 (2018).
[4] M. V. Morkovin, E. Reshotko, and T. Herbert, "Transition in open flow systems: A reassessment," Bull. APS **39**, 1–31 (1994).
[5] E. Reshotko, "Transition issues for atmospheric entry," J. Spacecr. Rockets **45**, 161–164 (2008).

[6]P. J. Schmid, "Nonmodal stability theory," Annu. Rev. Fluid Mech. **39**, 129–162 (2006).
[7]M. V. Morkovin, "On the many faces of transition," in *Viscous Drag Reduction* (Plenum, 1969), pp. 1–31.
[8]M. E. Goldstein, "Scattering of acoustic waves into Tollmien-Schlichting waves by small streamwise variations in surface geometry," J. Fluid Mech. **154**, 509–529 (1985).
[9]A. I. Ruban, "On Tollmien-Schlichting wave generation by sound," in *Laminar-Turbulent Transition*, edited by V. V. Kozlov (Springer Berlin Heidelberg, Berlin, Heidelberg, 1985), pp. 313–320.
[10]V. N. Zhigulev and A. V. Fedorov, "Boundary-layer receptivity to acoustic disturbances," J. Appl. Mech. Tech. Phys. **28**, 28–34 (1987).
[11]M. Choudhari and C. L. Streett, "A finite Reynolds-number approach for the prediction of boundary-layer receptivity in localized regions," Phys. Fluids A **4**(11), 2495–2514 (1992).
[12]M. E. Goldstein and L. S. Hultgren, "Boundary-layer receptivity to long-wave free-stream disturbances," Annu. Rev. Fluid Mech. **21**, 137–166 (1989).
[13]W. S. Saric, H. L. Reed, and E. J. Kerschen, "Boundary-layer receptivity to freestream disturbances," Annu. Rev. Fluid Mech. **34**, 291–319 (2002).
[14]L. M. Mack, "Linear stability theory and the problem of supersonic boundary-layer transition," AIAA J. **13**, 278–289 (1975).
[15]J. M. Kendall, "Wind tunnel experiments relating to supersonic and hypersonic boundary-layer transition," AIAA J. **13**, 290–299 (1975).
[16]K. F. Stetson, R. L. Kimmel, E. R. Thompson, J. C. Donaldson, and L. G. Siler, "A comparison of planar and conical boundary layer stability and transition at a Mach number of 8," AIAA Paper No. 91-1639, 1991.
[17]A. V. Fedorov and A. P. Khokhlov, "Prehistory of instability in a hypersonic boundary layer," Theor. Comput. Fluid Dyn. **14**, 359–375 (2001).
[18]Y. Ma and X. Zhong, "Receptivity of a supersonic boundary layer over a flat plate. Part 1. Wave structures and interactions," J. Fluid Mech. **488**, 31–78 (2003).
[19]A. Fedorov and A. Tumin, "High-speed boundary-layer instability: Old terminology and a new framework," AIAA J. **49**, 1647–1657 (2011).
[20]A. V. Fedorov, "Receptivity of a high-speed boundary layer to acoustic disturbances," J. Fluid Mech. **491**, 101–129 (2003).
[21]A. A. Maslov, A. N. Shiplyuk, A. A. Sidorenko, and D. Arnal, "Leading-edge receptivity of a hypersonic boundary layer on a flat plate," J. Fluid Mech. **426**, 73–79 (2001).
[22]Y. Ma and X. Zhong, "Receptivity of a supersonic boundary layer over a flat plate. Part 2. Receptivity to free-stream sound," J. Fluid Mech. **488**, 79–121 (2003).
[23]M R Malik and P. Balakumar, "Receptivity of supersonic boundary layers to acoustic disturbances," AIAA Paper No. 05-5027, 2005.
[24]I. V. Egorov, A. V. Fedorov, and V. G. Soudakov, "Receptivity of a hypersonic boundary layer over a flat plate with a porous coating," J. Fluid Mech. **601**, 165–187 (2008).
[25]P. Balakumar, "Receptivity of a supersonic boundary layer to acoustic disturbances," AIAA J. **47**, 1069–1078 (2009).
[26]E. J. Kerschen, "Boundary layer receptivity," AIAA Paper No. 89-1109, 1989.
[27]A. V. Fedorov and A. P. Khokhlov, "Receptivity of hypersonic boundary layer to wall disturbances," Theor. Comput. Fluid Dyn. **15**, 231–254 (2002).
[28]J. O. Pralits, C. Airiau, A. Hanifi, and D. S. Henningson, "Sensitivity analysis using adjoint parabolized stability equations for compressible flows," Flow, Turbul. Combust. **65**, 321–346 (2000).
[29]X. Wang and X. Zhong, "Effect of wall perturbations on the receptivity of a hypersonic boundary layer," Phys. Fluids **21**, 044101 (2009).
[30]X. Wang, X. Zhong, and Y. Ma, "Response of a hypersonic boundary layer to wall blowing-suction," AIAA J. **49**, 1336–1353 (2011).
[31]A. Tumin, "Multimode decomposition of spatially growing perturbations in a two-dimensional boundary layer," Phys. Fluids **15**, 2525–2540 (2003).
[32]A. Tumin, "Three-dimensional spatial normal modes in compressible boundary layers," J. Fluid Mech. **586**, 295–322 (2007).
[33]P. Gaydos and A. Tumin, "Multimode decomposition in compressible boundary layers," AIAA J. **42**, 1115–1121 (2004).
[34]A. Tumin, X. Wang, and X. Zhong, "Direct numerical simulation and the theory of receptivity in a hypersonic boundary layer," Phys. Fluids **19**, 014101 (2007).
[35]A. Tumin, X. Wang, and X. Zhong, "Numerical simulation and theoretical analysis of perturbations in hypersonic boundary layers," AIAA J. **49**, 463–471 (2011).
[36]A. Tumin, "Receptivity of compressible boundary layers to three-dimensional wall perturbations," AIAA Paper No. 06-1110, 2006.
[37]T. C. Corke, C. L. Enloe, and S. P. Wilkinson, "Dielectric barrier discharge plasma actuators for flow control," Annu. Rev. Fluid Mech. **42**, 505–529 (2010).
[38]S. B. Leonov, I. V. Adamovich, and V. R. Soloviev, "Dynamics of near-surface electric discharges and mechanisms of their interaction with the airflow," Plasma Sources Sci. Technol. **25**, 063001 (2016).
[39]P. C. Dörr and M. J. Kloker, "Crossflow transition control by upstream flow deformation using plasma actuators," J. Appl. Phys. **121**, 063303 (2017).
[40]Z. Guo and M. J. Kloker, "Control of crossflow-vortex-induced transition by unsteady control vortices," J. Fluid Mech. **871**, 427–449 (2019).
[41]Z. Guo and M. J. Kloker, "Effects of low-frequency noise in crossflow transition control," AIAA J. **58**, 1068–1078 (2020).
[42]C. Y. Schuele, T. C. Corke, and E. Matlis, "Control of stationary cross-flow modes in a Mach 3.5 boundary layer using patterned passive and active roughness," J. Fluid Mech. **718**, 5–38 (2013).
[43]A. Arndt, T. C. Corke, E. Matlisz, and M. Semper, "Controlled stationary/traveling cross-flow mode interaction in Mach 6 boundary layer," AIAA Paper No. 20-2058, 2020.
[44]M. A. Keller, M. J. Kloker, S. V. Kirilovskiy, P. A. Polivanov, A. A. Sidorenko, and A. A. Maslov, "Study of flow control by localized volume heating in hypersonic boundary layers," CEAS Space J. **6**, 119–132 (2014).
[45]Y. Wang, Y. Li, L. Xiao, B. Zhang, and Y. Li, "Similarity-solution-based improvement of γ-$Re_{\theta t}$ model for hypersonic transition prediction," Int. J. Heat Mass Transfer **124**, 491–503 (2018).
[46]S. P. G. Dinavahi, C. D. Pruett, and T. A. Zang, "Direct numerical simulation and data analysis of a Mach 4.5 transitional boundary-layer flow," Phys. Fluids **6**, 1323–1330 (1994).
[47]Y. Liu, M. Dong, and X. Wu, "Generation of first Mack modes in supersonic boundary layers by slow acoustic waves interacting with streamwise isolated wall roughness," J. Fluid Mech. **888**, A10 (2020).
[48]X. Li, D. Fu, and Y. Ma, "Direct numerical simulation of hypersonic boundary layer transition over a blunt cone," AIAA J. **46**, 2899–2913 (2008).
[49]X. Li, D. Fu, and Y. Ma, "Direct numerical simulation of hypersonic boundary layer transition over a blunt cone with a small angle of attack," Phys. Fluids **22**, 025105 (2010).
[50]M. R. Malik, "Numerical methods for hypersonic boundary layer stability," J. Comput. Phys. **86**, 376–413 (1990).
[51]T. Herbert, "Parabolized stability equations," Annu. Rev. Fluid Mech. **29**, 245–283 (1997).
[52]Y.-m. Zhang and H. Zhou, "Verification of parabolized stability equations for its application to compressible boundary layers," Appl. Math. Mech. **28**, 987–998 (2007).
[53]F. Li and M. R. Malik, "On the nature of PSE approximation," Theor. Comput. Fluid Dyn. **8**, 253–273 (1996).
[54]P. Andersson, D. S. Henningson, and A. Hanifi, "On a stabilization procedure for the parabolic stability equations," J. Eng. Math. **33**, 311–332 (1998).
[55]C.-L. Chang and M. R. Malik, "Oblique-mode breakdown and secondary instability in supersonic boundary layers," J. Fluid Mech. **273**, 323–360 (1994).
[56]J. Gao and J.-s. Luo, "Mode decomposition of nonlinear eigenvalue problems and application in flow stability," Appl. Math. Mech. **35**, 667–674 (2014).
[57]P. Balakumar and M. R. Malik, "Discrete modes and continuous spectra in supersonic boundary layers," J. Fluid Mech. **239**, 631 (1992).
[58]I. Maden, R. Maduta, J. Kriegseis, S. Jakirlić, C. Schwarz, S. Grundmann, and C. Tropea, "Experimental and computational study of the flow induced by a plasma actuator," Int. J. Heat Fluid Flow **41**, 80–89 (2013).
[59]P. C. Dörr and M. J. Kloker, "Numerical investigation of plasma-actuator force-term estimations from flow experiments," J. Phys. D: Appl. Phys. **48**, 395203 (2015).
[60]J. Little, K. Takashima, M. Nishihara, I. Adamovich, and M. Samimy, "Separation control with nanosecond-pulse-driven dielectric barrier discharge plasma actuators," AIAA J. **50**, 350–365 (2012).

[61] D. V. Roupassov, A. A. Nikipelov, M. M. Nudnova, and A. Y. Starikovskii, "Flow separation control by plasma actuator with nanosecond pulsed-periodic discharge," AIAA J. **47**, 168–185 (2009).
[62] V. Soloviev and V. Krivtsov, "Analytical and numerical estimation of the body force and heat sources generated by the surface dielectric barrier discharge powered by alternating voltage," in EUCASS 2015 VI European Conference for Aeronautics and Space Science, 2015.
[63] Y. Zhu and S. Starikovskaia, "Fast gas heating of nanosecond pulsed surface dielectric barrier discharge: Spatial distribution and fractional contribution from kinetics," Plasma Sources Sci. Technol. **27**, 124007 (2018).
[64] C. Li and Y. Zhang, "Effect of glow discharge on hypersonic flat plate boundary layer," Appl. Math. Mech. **40**, 249–260 (2019).
[65] C. Li, Y. Zhang, and C. Lee, " Influence of glow discharge on evolution of disturbance in a hypersonic boundary layer: The effect of first mode," Phys. Fluids **32**, 051701 (2020).